Nano Research Energy

ISSN 2791-0091 (print); 2790-8119 (online)
https://doi.org/10.26599/NRE.2026.9120264

Research Article

Gradient delocalized 4f-2p-3d orbital cascade of Gd-O-Mn sites remolding interfacial electronic landscape for accelerated Li-CO_2 batteries redox kinetics

Qinghua Deng[1] (✉), Husheng Tang[1], Yujie Qiang[2], Huaqing Liu[3], and Yahui Wu[4] (✉)

[1] *Wuhu R & D Center for Energy Conversion and Storage Materials, Wuhu Vocational Technical University, Wuhu 241002, China*
[2] *Key Laboratory of Functional Molecular Solids, Ministry of Education, Anhui Normal University, Wuhu 241002, China*
[3] *Faculty of Life and Environmental Sciences, University of Tsukuba, Tsukuba, Ibaraki, 3058577, Japan*
[4] *School of Pharmacy, Bengbu Medical University, Bengbu 233030, China*

Received: 2 July 2026 / **Revised:** 4 August 2026 / **Accepted:** 11 August 2026 / **Published date:** 7 September 2026

ABSTRACT

Conventional transition-metal cathodes constrained by a limited 3d-2p orbital manifold suffer from an unfavorable electronic structure that impedes the electrochemical kinetics of Li-CO_2 batteries. Incorporating rare-earth 4f orbitals introduces strong spin-orbit coupling and a delocalized f-p-d cascade, fundamentally remolding interfacial electronic landscape. Herein, asymmetric Gd-O-Mn active sites are constructed via a 4f-2p-3d gradient orbital coupling strategy by doping gadolinium into Mn_3O_4 nanorods. This establishes a cascaded Gd 4f-O 2p-Mn 3d electronic conduit inducing directional charge redistribution and augmented electron density. The electropositive Gd dopant simultaneously elevates the O 2p band center and activates lattice oxygen redox chemistry, facilitating both the nucleophilic attack on CO_2 and the subsequent cleavage of carbonate bonds. Consequently, the Gd-Mn_3O_4 cathode delivers an exceptional full discharge capacity of 14,640 mAh·g^{-1}, a remarkably low overpotential of 1.23 V, and extended cycling stability over 230 cycles. Comprehensive experimental and theoretical analyses reveal the f-p-d cascade coupling not only preserves the structural integrity of the MnO_6 framework but also optimizes the adsorption energetics of key intermediates $^*C_2O_4$. This work elucidates the mechanistic role of gradient orbital hybridization in stabilizing manganese-based cathodes and offers a new paradigm for the rational design of advanced catalytic sites in Li-CO_2 batteries cathodes.

KEYWORDS

Li-CO_2 batteries, catalytic cathode, 4f electrons, gradient orbital coupling, Gd-Mn_3O_4

1 Introduction

The unsustainable combustion of fossil fuels drives the continuous increase in atmospheric carbon dioxide (CO_2) concentration, which severely endangers the global ecological balance. To address global warming and climate change, the development of carbon neutrality technologies, especially carbon capture, utilization and storage (CCUS) technologies for CO_2, has become a critical strategy to tackle global climate challenges [1–3]. The Li-CO_2 battery, a novel energy storage device with a high theoretical energy density of 1876 Wh·kg^{-1}, has attracted extensive attention among various CCUS technologies owing to its capability of efficiently converting greenhouse gas CO_2 into sustainable electric energy [4]. Li-CO_2 batteries operate based on the reversible reaction: $4Li^+ + 4e^- + 3CO_2 \leftrightarrow 2Li_2CO_3 + C$, with a discharge voltage of 2.85 V (vs. Li^+/Li) [5]. The discharge process involves the activation and reduction of CO_2, generating insulate and inert discharge product Li_2CO_3. This gradually accumulated product clogs the mass/charge transport channels, leading to a rapid decay in discharge-recharge performance [6, 7]. To enhance the output power during discharge, reduce the recharging voltage and improve cycling stability, researchers have devoted intensive efforts to developing advanced catalytic cathode materials, which enable the timely and efficient reduction of CO_2. Representative catalytic materials include carbon-based materials, noble metals, transition metals, organic crystalline materials, MXene and so on [8–10].

Among them, transition metal compounds (such as cobalt, manganese, molybdenum, and nickel) are widely recognized as possessing superior application potential in cathode systems for Li-CO_2 batteries, owing to their partially filled d-orbitals, abundant and tunable valence states, and favorable processability [11–15]. Notably, manganese-based oxides have attracted extensive attention due to their high discharge voltage, abundant natural reserves, and excellent environmental compatibility [16–18].

Address correspondence to Qinghua Deng, 101458@whit.edu.cn; Yahui Wu, wuyah2025@bbmu.edu.cn

Nevertheless, Mn^{4+} ions are prone to reduction under the high-voltage conditions during recharging, which triggers the structural decomposition of [MnO_6] octahedra and consequently leads to capacity fading [19–21]. This issue severely restricts the practical application of manganese-based oxides in Li-CO_2 batteries. To tackle the structural degradation and sluggish redox kinetics of Mn-based Li-CO_2 cathodes, multiple modification approaches such as heteroatom doping, heterostructure design and high-entropy engineering have been proposed in previous studies [4, 8]. Most reported strategies, however, merely rely on conventional d-p orbital modulation for Mn-based catalysts, while single d-p hybridization cannot create a flexible orbital environment to adapt dynamic electron redistribution under varying cycling voltages, and the large energy mismatch between Mn 3d and O 2p orbitals inevitably restricts catalytic activity and long-term stability [22–24]. The significant energy difference between the 3d and O 2p orbitals are the primary causes of this limitation. Therefore, there is an urgent need to develop an unconventional electronic state regulation strategy based on orbital hybridization.

Considering that rare-earth (RE) elements possess tunable valence states, strong spin-orbit coupling, and adjustable positions of their 4f energy levels relative to the Fermi level (E_f), their integration into manganese oxide systems enables valence electron transfer across gradient orbitals [25–27]. This process induces pronounced surface spin polarization. Combining rare-earth 4f orbitals with transition metal M-O bonds can establish a unique RE 4f-O 2p-M 3d gradient orbital coupling framework, which outperforms the conventional single d-p modulation widely adopted in previous Mn-based and rare-earth modified catalysts. This multi-orbital structure greatly expands the adjustable range of electronic states and manipulates spin-related electron transport paths, strengthening spin-orbit interactions between metal sites and reaction intermediates [28–30]. Distinct from simple rare-earth doping schemes reported earlier, this f-p-d cascade system can precisely tune e_g orbital filling to boost bidirectional redox kinetics of Li-CO_2 batteries [23, 31]. Additionally, rare-earth-containing nanomaterials with abundant exposed active sites can construct atomic-level asymmetric Gd-O-Mn motifs. Such asymmetric coordination accelerates charge migration during cycling and alleviates the Jahn-Teller distortion-induced breakdown of MnO_6 octahedra, a critical defect limiting the lifespan of ordinary Mn-based cathodes [19, 23, 24]. Collectively, these features suggest that asymmetric active sites with f-p-d orbital gradient coupling offer substantial advantages in electrochemical reaction processes, representing a promising strategy for enhancing battery performance. Nevertheless, the strongly localized nature of RE 4f orbitals generally precludes their direct participation in covalent bonding interactions [32–34]. Consequently, prior rare-earth modified Mn-based cathodes mainly concentrate on simple morphological or electronic optimization, and few works systematically reveal how rare-earth 4f orbitals participate in catalytic cycles. This insufficient fundamental cognition severely restricts the targeted structural design of high-efficiency Mn-based cathodes and deep mechanistic interpretation of reversible CO_2 redox reactions.

Based on the above considerations, we herein report the incorporation of gadolinium (Gd) into manganese oxide (Mn_3O_4) nanorods to construct asymmetric Gd-O-Mn active sites through a gradient orbital coupling pathway involving RE 4f, O 2p, and Mn 3d orbitals for application in Li-CO_2 batteries. Benefiting from the spin-orbit coupling between these asymmetric sites and key intermediates during discharge-recharge processes, the structural integrity of the MnO_6 framework is markedly enhanced, leading to substantially improved electrochemical performance. The resulting Li-CO_2 battery delivers an exceptional full discharge capacity of 14,640 mAh·g^{-1}, a remarkably low overpotential of 1.23 V, and extended cycling stability over 230 cycles. Furthermore, comprehensive experimental investigations combined with theoretical calculations reveal that the introduction of Gd reinforces the electronic structure and bonding characteristics of Mn-O units throughout the discharge-recharge process. This work not only demonstrates the effectiveness of f-p-d orbital gradient coupling in stabilizing manganese-based cathodes, but also provides a new paradigm for the rational design of active sites in advanced catalytic cathodes for Li-CO_2 batteries.

2 Experimental

2.1 Electrocatalysts preparation

Gd-doped Mn_3O_4 (denoted as Gd-Mn_3O_4) was synthesized via a solvothermal method followed by high-temperature calcination. Typically, 2 mmol of manganese (II) acetate, 0.2 mmol of gadolinium (III) nitrate, and 3 mmol of 1,3,5-benzenetricarboxylic acid were dissolved in 80 mL of methanol under continuous stirring. After stirring for 1 h, the mixture was transferred and refluxed at 80 °C for 24 h under magnetic stirring. The product was collected by centrifugation at 8000 rpm·min^{-1} after naturally cooling down to room temperature, and alternately washed with ethanol and deionized water several times. The obtained precipitate was freeze-dried and then calcined in a tube furnace at 500 °C for 2 h under a N_2 atmosphere with a heating rate of 5 °C·min^{-1}. For comparison, pure Gd_2O_3 and Mn_3O_4 were prepared under identical synthetic procedures without the addition of manganese and gadolinium sources, respectively.

2.2 Characterizations

The physicochemical properties and microstructure of the as-prepared electrocatalysts were investigated using a series of complementary characterization techniques. Powder X-ray diffraction (XRD) patterns were recorded on a Bruker D8 diffractometer with Cu K_α radiation (λ = 1.541 Å). Raman spectra were obtained on a LabRAM HR spectrometer over the range of 100–1000 cm^{-1}. Electron paramagnetic resonance (EPR) measurements to identify oxygen vacancies were carried out using a Bruker EMXplus spectrometer. Nitrogen physisorption isotherms were measured on an ASAP 2460 analyzer to determine the specific surface area and pore structure. Morphological and microstructural observations were performed via scanning electron microscopy (SEM, JEOL JSM-5600L) and transmission electron microscopy (TEM), including high-resolution TEM (HRTEM) on a JEM-2010 instrument. Surface chemical states and elemental compositions were analyzed by X-ray photoelectron spectroscopy (XPS) on a Thermo Scientific ESCALAB 250Xi system, with all binding energies calibrated against the C 1s peak at 284.8 eV. X-ray absorption spectroscopy (XAS) experiments, including both near-edge (XANES) and extended fine structure (EXAFS) regions, were conducted at the BL14W1 beamline of the Shanghai Synchrotron Radiation Facility (SSRF), operating at an electron energy of 3.5 GeV and a storage current of 300 mA. A Si(111) double-crystal monochromator was used for energy selection. The acquired XAS data were processed and fitted using the IFFEFIT 1.2.11 package (incorporating Athena and Artemis). Fourier-transform infrared (FT-IR) spectra were collected on a

NEXUS470 spectrophotometer using KBr pellets. The evolution of gaseous species during electrochemical reactions was monitored by *in situ* differential electrochemical mass spectrometry (*in situ* DEMS), employing a home-built system integrated with an electrochemical workstation and a Pfeiffer Vacuum QMS 200 mass spectrometer.

2.3 Li-CO_2 batteries assembly

All electrochemical measurements were conducted at 25 °C in a dry CO_2 atmosphere. The Li-CO_2 batteries were assembled as CR2032-type coin cells featuring perforated cathodes. Cell fabrication took place inside an argon-filled glovebox using ultra-high purity argon. Catalytic cathodes were prepared prior to assembly. A cathode ink was first prepared by accurately weighing and dispersing the active material, Super P, and a binder in N-methyl-2-pyrrolidone (NMP) at a mass ratio of 10:3:3. The resulting slurry was evenly spread and uniformly distributed onto a carbon paper current collector, serving as a gas diffusion electrode. After coating, the electrode was dried at 60 °C and subsequently accurately punched into discs of 14 mm diameter. Glass fiber separators (18 mm diameter) and lithium metal anodes (16 mm diameter) were precisely tailored for assembly. An electrolyte volume of 80 μL of 1 M $LiCF_3SO_3$ dissolved in TEGDME was carefully dispensed between the electrodes to ensure lithium-ion conduction. The cells were sealed with a crimping machine and then left to rest in a dry CO_2 environment for more than 12 hours. A low-current aging and formation step was applied before formal testing. The active material loading on the catalytic cathode was maintained at approximately 0.35 mg·cm^{-2}, which served as the basis for calculating current densities. Galvanostatic charge and discharge profiles were recorded on a LAND CT3002A battery test system (Wuhan LAND Electronics) under either voltage-limited or capacity-limited conditions. Cyclic voltammetry (CV) and electrochemical impedance spectroscopy (EIS) were performed on a CHI760E workstation (CH Instruments, Shanghai). CV curves were acquired between 2.0 V and 4.3 V at a scan rate of 0.1 mV·s^{-1}. EIS measurements were carried out over a frequency range from 1 MHz to 0.1 Hz with an AC amplitude of 5 mV.

3 Results and discussion

The substitutional doping of Gd^{3+} into the Mn_3O_4 matrix preferentially occurs at octahedral Mn^{3+} sites, constructing discrete Gd-O-Mn linkages that drastically reshape the local electronic landscape (Fig. 1) [35, 36]. Mn_3O_4 adopts a normal spinel structure containing tetrahedral high-spin Mn^{2+} (d^5) and octahedral high-spin Mn^{3+} (d^4). Octahedral Mn^{3+} intrinsically undergoes Jahn-Teller distortion, breaking octahedral crystal field degeneracy and splitting Mn 3d e_g orbitals into separate dz^2 and dx^2-y^2 sub-states [19, 37]. Upon Gd^{3+} ($4f^7$) incorporation, the larger ionic radius of Gd triggers local lattice expansion, disrupting cooperative Jahn-Teller ordering and forming an anisotropic ligand environment around Gd centers. The half-filled Gd 4f orbitals are fully shielded by closed $5s^25p^6$ shells and remain highly localized without direct covalent bonding with oxygen; nevertheless, Gd doping modulates electronic properties via two distinct orbital pathways. Empty Gd 5d orbitals dominate static covalent orbital coupling. The electropositive Gd redistributes the Madelung potential across Gd-O-Mn units and shifts the O 2p band center toward the Fermi level. Vacant Gd 5d orbitals hybridize with O 2p states, which further covalently couple with Mn 3d t_{2g} and e_g manifolds to form a steady Mn 3d-O 2p-Gd 5d electronic conduit, creating a delocalized charge network that drives electron transfer from Gd to Mn. In contrast, localized Gd 4f orbitals deliver exclusive dynamic spin regulation via strong

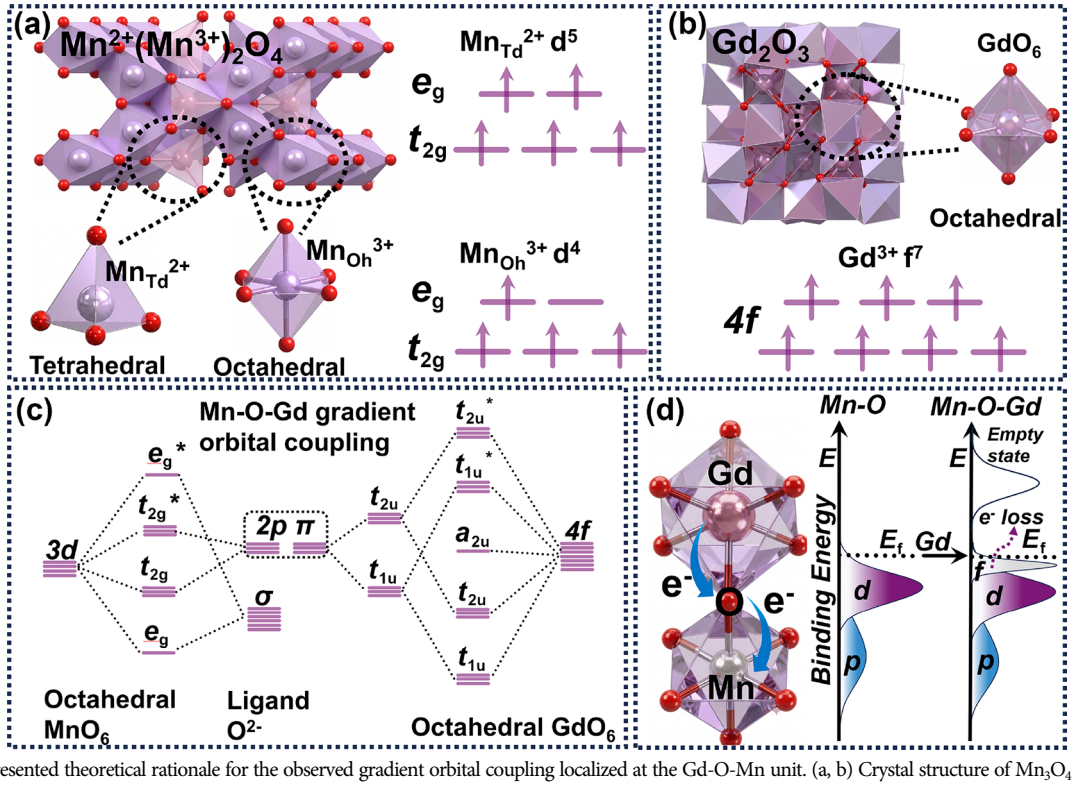

Figure 1 A presented theoretical rationale for the observed gradient orbital coupling localized at the Gd-O-Mn unit. (a, b) Crystal structure of Mn_3O_4 and Gd_2O_3. (c) The qualitative energy-level correlation diagram obtained for the MnO_6 and GdO_6 units with an Oh symmetry. (d) Formation of d-p-f gradient orbital coupling with electron buffering from the f band.

spin-orbit coupling—an effect unachievable by Mn 3d, O 2p or Gd 5d alone. Gd 4f orbitals induce interfacial spin polarization and serve as electron buffers to accommodate transient excess charge during cyclic redox reactions [32, 38–40]. Driven by stronger electro-positivity of Gd relative to Mn, electron density accumulates on bridging lattice oxygen, raising its anionic charge and shifting Mn-O bonding toward an ionic character, endows Gd-O-Mn motifs with bifunctional catalytic activity for reversible Li-CO_2 redox. During discharge, O 2p-Mn t_{2g} hybridization builds a π-symmetric electron transport channel, improves energy alignment with $2\pi_u$ antibonding orbital of CO_2 [16, 41, 42].

This symmetry-matched orbital interaction accelerates electron injection into CO_2, lowering the nucleophilic attack barrier and facilitating Li_2CO_3 generation. Upon recharge, the enriched electron density on lattice oxygen strengthens its nucleophilicity to directly cleave carbonate C-O bonds. Meanwhile, Gd-induced lattice distortion modulates Mn-O bond strength and reduces the activation enthalpy for oxygen migration, promoting full decomposition of insulating Li_2CO_3 [23, 24]. Collectively, the static charge transfer mediated by Gd 5d-O 2p-Mn 3d coupling and the dynamic spin buffering of Gd 4f orbitals work synergistically to optimize bidirectional redox kinetics and activate lattice oxygen redox, affording the Gd-Mn_3O_4 cathode mitigated overpotential and outstanding cycling stability for Li-CO_2 batteries.

The Gd-Mn_3O_4 nanorod catalyst was synthesized via a self-assembly mediated precursor route followed by a controlled thermal annealing step, as schematically illustrated in Fig. 2(a). The phase constitution and crystallographic evolution of the as-prepared samples were examined by XRD as presented in Fig. 2(b) and Table S1 in the Electronic Supplementary Material (ESM). For the pristine Mn_3O_4 component, the diffraction pattern exhibits a characteristic tetragonal structure (PDF #24-0734) with distinct reflections indexed to the (101), (112), (103), (211), (220), (105), (321), and (400) planes [43]. In the case of the Gd_2O_3 reference, a cubic bixbyite-type phase is observed, displaying prominent peaks assignable to the (222), (400), (440), and (622) crystallographic planes (PDF #12-0797) [44]. Notably, the diffraction profile of the Gd-Mn_3O_4 composite retains the principal reflection positions of the tetragonal Mn_3O_4 matrix, indicating that the long-range periodic framework of the spinel host is substantially preserved upon gadolinium incorporation. However, a conspicuous broadening of the full width at half maximum is evident across all diffraction features of Gd-Mn_3O_4 relative to pristine Mn_3O_4. This systematic peak broadening provides direct crystallographic evidence for a dopant-induced lattice distortion, consistent with the generation of micro-strain and a reduction in coherent domain size arising from the ionic radius mismatch between Gd^{3+} and the native octahedral Mn^{3+} site [20, 45].

To further elucidate the local structural perturbations imparted by Gd incorporation, Raman spectroscopy and EPR measurements were performed, as displayed in Figs. 2(c) and 2(d). Compared with pristine Mn_3O_4, the Gd-Mn_3O_4 sample exhibits an obvious red shift of Mn-O octahedral stretching vibrations, alongside emerged low-frequency vibrational band at ~142 cm^{-1} originating from coupled Gd-O oscillations within the Gd-O-Mn bridging units. This softening of the lattice vibrations corroborates a weakening of the metal-oxygen bond force constants and is fully consistent with the expanded and distorted coordination environment induced by the larger Gd^{3+} cation [21, 46]. Complementarily, the EPR spectrum of Gd-Mn_3O_4 exhibits a

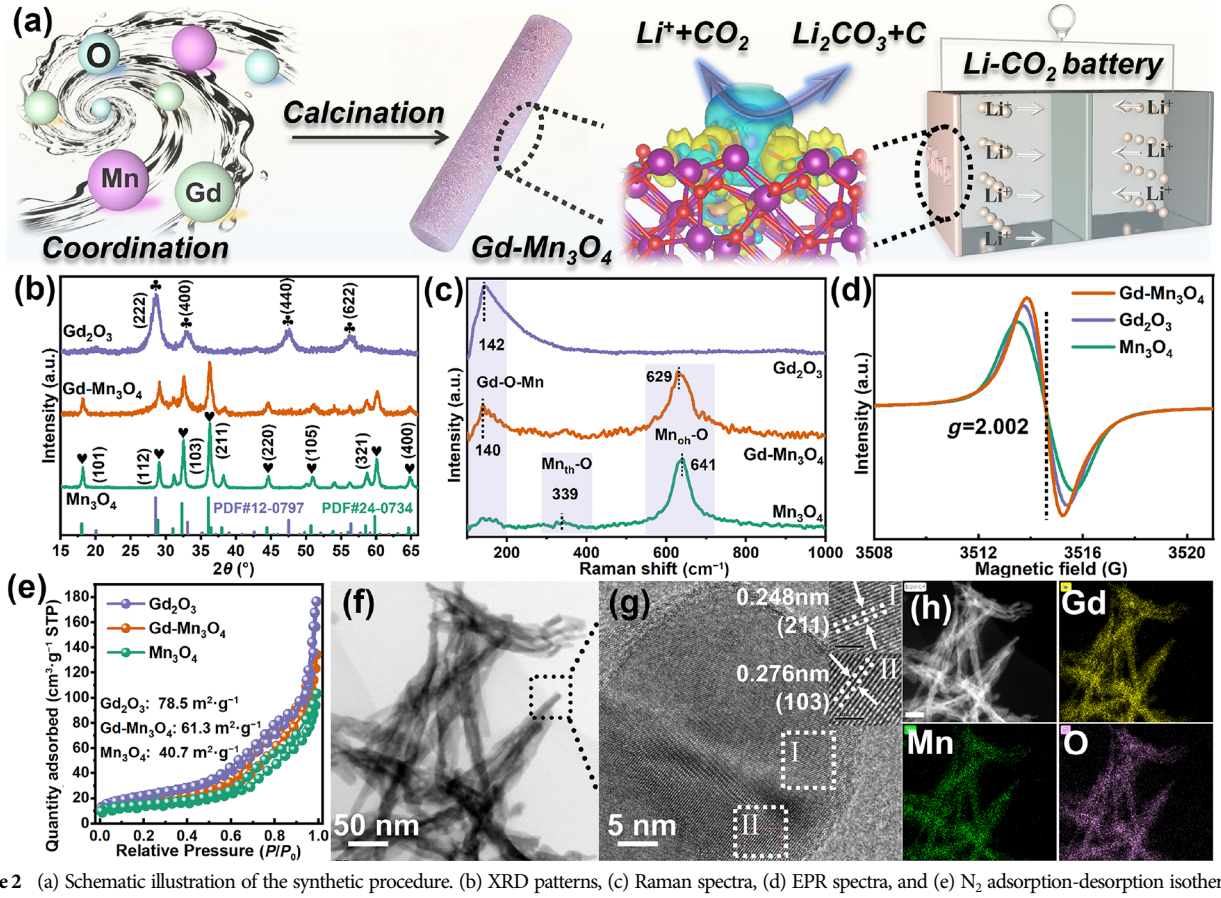

Figure 2 (a) Schematic illustration of the synthetic procedure. (b) XRD patterns, (c) Raman spectra, (d) EPR spectra, and (e) N_2 adsorption-desorption isotherms of the prepared samples. (f, g) TEM and HRTEM images of the Gd-Mn_3O_4 sample, and (h) the corresponding EDS elemental mapping images.

marked enhancement in signal intensity relative to pristine Mn_3O_4. Given that pristine Mn_3O_4 intrinsically hosts high-spin Mn^{2+} and Mn^{3+} centers, the pronounced enhancement of the paramagnetic EPR signal for Gd-Mn_3O_4 confirms a higher concentration of unpaired electrons, which stems from two doping-induced factors: the formation of oxygen vacancies and symmetry distortion of MnO_6 octahedra upon Gd substitution. Together, these spectroscopic signatures unambiguously validate the Gd-induced lattice distortion deduced from XRD analysis [23]. Furthermore, nitrogen adsorption desorption isotherms and the corresponding pore-size distribution profiles (Fig. 2(e), Fig. S1 in ESM) verify that the Gd-Mn_3O_4 nanorods deliver a large specific surface area, which enables abundant exposure of catalytic interfacial active sites. The uniform pore size at ~7.5 nm provides unobstructed channels to accelerate electrolyte and CO_2 mass transport throughout the Li-CO_2 redox process.

TEM was further employed to elucidate the morphological characteristics of the as-synthesized samples. As evidenced by Fig. S2 in the ESM and Fig. 2(f), pristine Gd_2O_3 exhibits an irregular nanoparticulate morphology with non-uniform size distribution, whereas the unmodified Mn_3O_4 sample displays well-defined nanorod architectures with a relatively uniform diameter of approximately 40 nm. In stark contrast, the Gd-Mn_3O_4 retains the nanorod morphology yet manifests a discernible reduction in the average rod diameter. This refinement in lateral dimension could be plausibly attributed to a gadolinium-induced attenuation of the kinetic nucleation barrier during the growth of the Mn_3O_4 crystallites [47, 48]. The reduced diameter is beneficial for exposing more active surface sites and facilitating the subsequent diffusion and migration of CO_2 molecules and electrolyte, a conclusion that is fully consistent with the specific surface area measurements discussed above. HRTEM examination further unveils the incorporation of Gd heteroatoms introduce a subtle yet unequivocal lattice distortion within the pristine Mn_3O_4 matrix, thereby establishing the requisite local structural prerequisites for the construction of asymmetric Gd-O-Mn coordination motifs [49]. Complementarily, EDS elemental mapping presented in Fig. 2(h) confirms a spatially homogeneous distribution of Gd, Mn, and O throughout the Gd-Mn_3O_4 nanorods, unambiguously attesting to the uniform integration of gadolinium species into the host oxide framework rather than the formation of discrete phase-segregated domains.

The formation of asymmetric Gd-O-Mn active sites and the modulation of the local electronic structure of Mn upon Gd incorporation were investigated by a combined synchrotron XAS and XPS. Figure 3(a) presents the normalized Gd L_3-edge XANES spectra. The absorption-edge position of Gd-Mn_3O_4 is nearly identical to those of Gd_2O_3, indicating that Gd retains a stable +3 oxidation state within the Mn_3O_4 matrix and is not reduced upon doping. Figure 3(b) and Fig. S4 in the ESM displays the Fourier transforms of the k^3-weighted Gd L_3-edge EXAFS spectra. Whereas Gd_2O_3 exhibits only the first-shell Gd-O coordination, Gd-Mn_3O_4 shows an additional second-shell feature at a radial distance of approximately 2.8 Å [32, 50]. Quantitative EXAFS fitting (Fig. 3(c) and Table S2 in the ESM) assigns this contribution to a Gd-O-Mn backscattering path with a coordination number of ~1.8 and an interatomic distance of roughly 3.2 Å, thereby providing direct evidence for the existence of Gd-O-Mn linkages. The Mn sublattice was further probed by Mn K-edge XAS to evaluate the structural consequences of Gd doping. As shown in Fig. 3(d), the Mn K-edge XANES of Gd-Mn_3O_4 is slightly shifted toward higher energy relative to that of

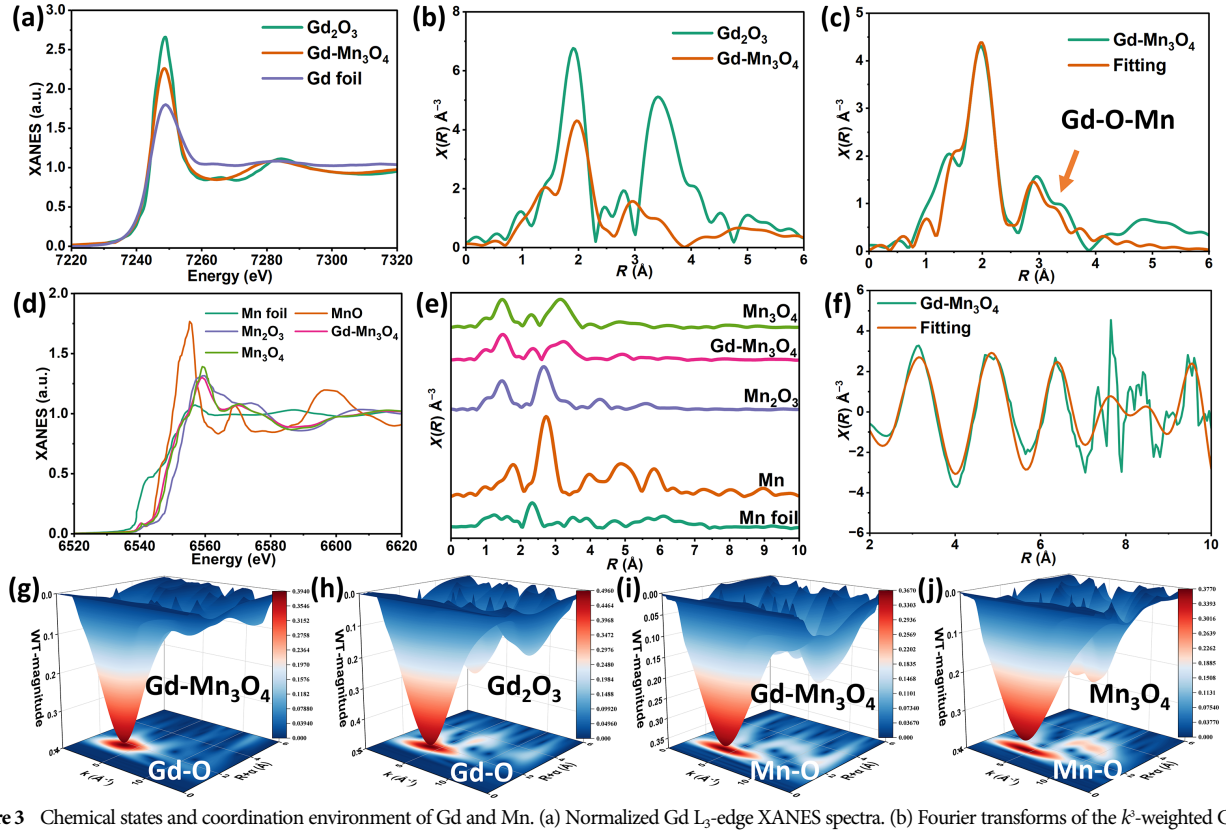

Figure 3 Chemical states and coordination environment of Gd and Mn. (a) Normalized Gd L_3-edge XANES spectra. (b) Fourier transforms of the k^3-weighted Gd L_3-edge EXAFS spectra, and (c) the corresponding fitting results for Gd-Mn_3O_4. (d) Normalized Mn K-edge XANES spectra. (e) Fourier transforms of the k^3-weighted Mn K-edge EXAFS spectra, and (f) the corresponding fitting results for Gd-Mn_3O_4. Wavelet transforms of the k^3-weighted EXAFS signals: (g, h) Gd L_3-edge for Gd-Mn_3O_4 and Gd_2O_3, respectively; (i, j) Mn K-edge for Gd-Mn_3O_4 and Gd_2O_3, respectively.

pristine Mn_3O_4. Such a shift is generally associated with alterations in local symmetry and crystal-field effects around Mn rather than a net increase in oxidation state, the latter being ruled out by the XPS results discussed below [51]. The Fourier-transformed EXAFS spectra (Fig. 3(e)) reveal that the first-shell Mn-O peak in Gd-Mn_3O_4 is attenuated and marginally displaced. Fitting analysis (Fig. 3(f)) yields a shortened Mn-O bond length and an enlarged Debye-Waller factor, confirming a local distortion of the MnO_6 octahedra induced by the larger Gd^{3+} cation. Notably, a second-shell Mn-Gd scattering contribution is also resolved, consistent with the heterometallic connectivity deduced from the Gd L_3-edge data. To discriminate amongbackscattering atoms, wavelet transform (WT) analysis of the k^3-weighted EXAFS signals was performed. For the Gd L_3-edge of the Gd-Mn_3O_4 (Fig. 3(g)), the first shell manifests as a single intensity maximum at a low k value (~4.5 $Å^{-1}$), characteristic of oxygen backscattering. This high-k feature is absent in the WT of Gd_2O_3 (Fig. 3(h)) and is typical of backscattering from a transition metal Mn. Analogously, the Mn K-edge WT of Gd-Mn_3O_4 (Fig. 3(i)) displays, in addition to the low-k Mn-O contribution, a high k feature attributable to Mn-Gd interactions, whereas no such feature is observed for pristine Mn_3O_4 (Fig. 3(j)). These WT results independently corroborate the Gd-O-Mn coordination motif [39, 52]. Surface electronic states were further examined by XPS (Fig. S3 in the ESM). The survey spectrum (Fig. S3(a) in the ESM) confirms the presence of Gd, Mn, O, and C. In the high-resolution Gd 4d spectrum (Fig. S3(b) in the ESM), Gd-Mn_3O_4 exhibits peaks at approximately 142.6 and 147.8 eV, corresponding to the Gd $4d_{5/2}$ and Gd $4d_{3/2}$ components, respectively, with no evidence of metallic Gd, consistent with a pure Gd^{3+} chemical state. Importantly, the Mn 2p spectrum (Fig. S3(c) in the ESM) reveals that the binding energies of Mn $2p_{3/2}$ and Mn $2p_{1/2}$ in Gd-Mn_3O_4 are shifted downward by 0.2 eV relative to pristine Mn_3O_4. This negative shift indicates an accumulation of electron density at the Mn sites upon Gd incorporation, implying that charge is transferred from Gd to Mn through the Gd-O-Mn bridge [53, 54]. This experimental observation is in excellent agreement with the density functional theory calculations presented subsequently. The O 1s spectrum (Fig. S3(d) in the ESM) can be deconvoluted into lattice oxygen and oxygen vacancies/surface-adsorbed oxygen species. Compared with pristine Mn_3O_4, the proportion of oxygen vacancies in Gd-Mn_3O_4 is significantly higher, a consequence of charge compensation accompanying the substitution of Mn^{3+} by Gd^{3+}. These oxygen vacancies additionally serve as active sites for CO_2 activation [55, 56]. Collectively, the synchrotron XAS and XPS results provide complementary and mutually reinforcing evidence: EXAFS and wavelet transform analyses unambiguously establish the atomic-scale Gd-O-Mn connectivity, whereas XPS reveals a Gd-to-Mn electron transfer that enriches the Mn sites with electron density. This redistribution of electronic charge, together with the local lattice distortion induced by the Gd-O-Mn configuration, constitutes a structural foundation for optimizing the kinetics of both CO_2 reduction and evolution reactions in Li-CO_2 batteries.

To experimentally validate the catalytic advantages conferred by the asymmetric Gd-O-Mn coordination architecture elucidated above, the Li-CO_2 batteries electrochemistry of the Gd-Mn_3O_4 nanorods was systematically interrogated and benchmarked against the pristine Mn_3O_4 and Gd_2O_3 reference systems. Figure 4(a) presents the comparative galvanostatic discharge and recharge profiles of the respective cathodes evaluated within a voltage window of 2.0–4.5 V at a current density of 100 $mA·g^{-1}$. Remarkably, the incorporation of gadolinium heteroatoms into the spinel host engenders a profound augmentation in the full discharge capacity, elevating it from a baseline value of 5589 $mAh·g^{-1}$ for pristine Mn_3O_4 to an exceptional 14,640 $mAh·g^{-1}$ for the Gd-Mn_3O_4. This near threefold enhancement in capacity is accompanied by a discernible thermodynamic and kinetic facilitation of the redox processes: the discharge plateau is shifted anodically from 2.44 to 2.61 V, while the corresponding recharge plateau is substantially depressed from 4.15 to 3.92 V. It is noteworthy that the electrochemical performance metrics of the discrete Gd_2O_3 phase remain markedly inferior to those of both the pristine and doped manganite systems, unequivocally demonstrating that the observed enhancements are not a trivial consequence of a composite effect but rather an emergent property stemming from the atomically intimate Gd-O-Mn interfacial linkages. These observations are fully consistent with the theoretical premise of an elevated O 2p band center and the enhanced nucleophilicity of lattice oxygen sites; the optimized energetic alignment between the O 2p-Mn t_{2g} π-conduit and the CO_2 $2_{\pi u}$ antibonding orbital effectively lowers the activation barrier for the initial nucleophilic attack, thereby facilitating deep discharge, while the augmented electron density on the bridging oxygen concurrently promotes the subsequent cleavage of the carbonate C-O bond during recharge, mitigating the accumulation of deleterious overpotential [4, 16, 41].

To further deconvolute the intrinsic kinetic polarization from the full depth of discharge, the voltage profiles were recorded at a curtailed fixed capacity of 1000 $mAh·g^{-1}$ at an identical current rate of 100 $mA·g^{-1}$, as displayed in Fig. 4(b). The incorporation of Gd results in a striking compression of the voltage hysteresis, which narrows from 1.80 V for the pristine Mn_3O_4 electrode to a mere 1.23 V for the Gd-Mn_3O_4 analogue. This substantial mitigation of overpotential provides direct experimental validation that the Gd-induced modulation of the Mn-O covalency toward a more ionic regime lowers the activation enthalpy for oxygen migration and expedites the decomposition of the discharge product. The attendant improvement in round-trip energy efficiency underscores the critical role of the activated lattice oxygen redox chemistry in rendering the evolution reaction more reversible. The robustness of the Gd-Mn_3O_4 catalytic interface under varying operational currents was next examined via a rate capability assessment, as shown in Fig. 4(c). Upon stepping the applied current density from 50 to 200 $mA·g^{-1}$, the Gd-Mn_3O_4 cathode maintains a highly competitive and stable discharge capacity with only a modest escalation in overpotential. This resilience against concentration polarization under high-flux conditions attests to the rapid charge-transfer kinetics facilitated by the Gd-O-Mn conduit and the expedited solid-state diffusion of Li^+ and CO_2 intermediates. Such rate capability is indicative of a catalyst architecture wherein the surface reaction kinetics, rather than mass transport limitations, dictate the overall performance envelope [16, 57].

CV was employed to further deconvolute the distinct faradaic processes associated with CO_2 reduction and evolution (Fig. 4(d), Fig. S5 in the ESM). In stark contrast to the ill-defined and kinetically sluggish responses of the pristine Mn_3O_4 and Gd_2O_3 electrodes, the Gd-Mn_3O_4 cathode exhibits markedly enhanced peak current densities for both the cathodic sweep and the anodic sweep. Notably, a well-defined and intense cathodic feature emerges at approximately 2.68 V, a potential window characteristic of the facilitated nucleophilic insertion of Li^+ into CO_2. The amplification of this reduction peak current

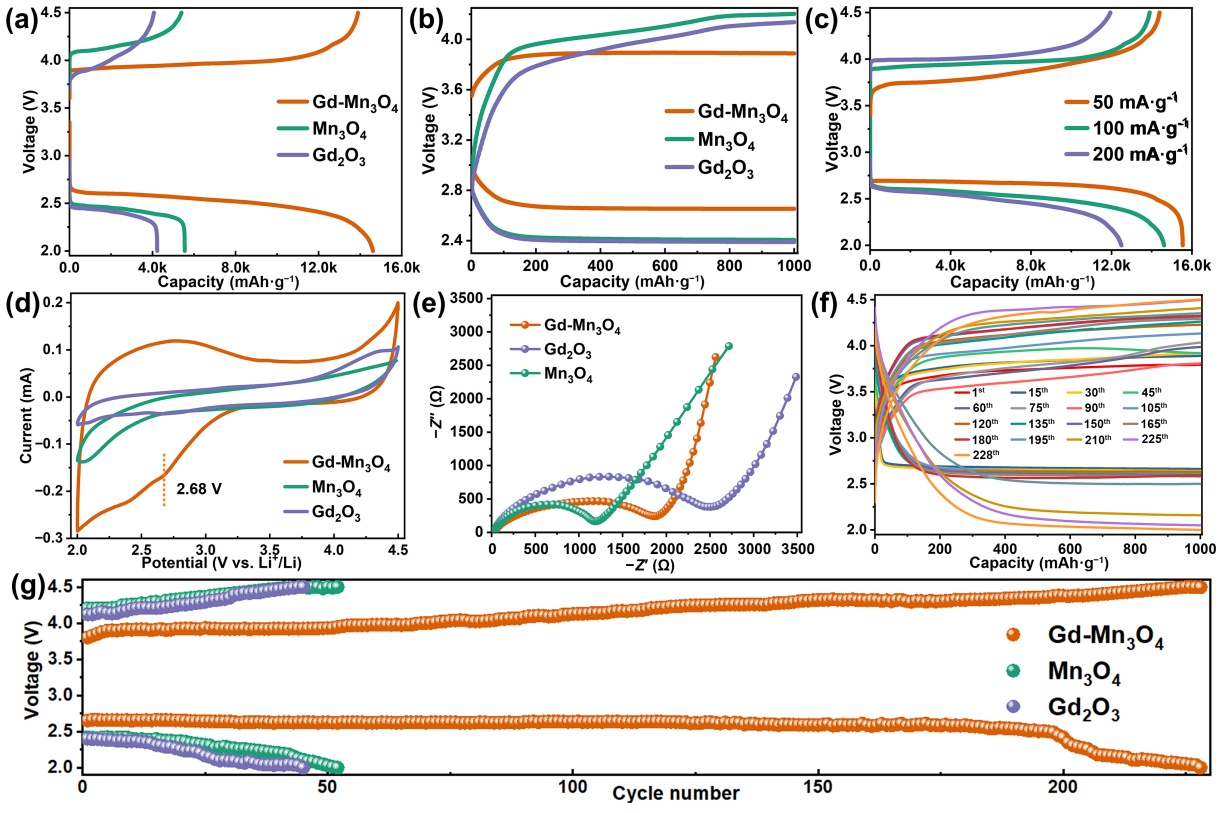

Figure 4 Electrochemical assessment of the as-assembled Li-CO_2 batteries. (a) Galvanostatic discharge-charge curves for different cathodes cycled between 2.0–4.5 V at 100 mA·g^{-1}. (b) Voltage profiles of various cathodes at a fixed capacity of 1000 mAh·g^{-1} and 100 mA·g^{-1}. (c) Rate performance of Gd-Mn_3O_4 electrodes at varied current densities within 2.0–4.5 V. (d) CV curves measured in CO_2 at 0.1 mV·s^{-1} from 2.0 to 4.5 V for different cathodes. (e) EIS data for the respective cathode materials. (f) Cycling stability of the Gd-Mn_3O_4 cathode at a cutoff capacity of 1000 mAh·g^{-1} and 100 mA·g^{-1}. (g) Terminal voltage variation over cycling for different cathodes under a 1000 mAh·g^{-1} capacity limit and 100 mA·g^{-1}.

corroborates the enhanced electron donation through the symmetry-matched π-conduit enabled by the Gd-O-Mn motifs, thereby lowering the energetic threshold for CO_2 activation. The corresponding anodic peak associated with carbonate decomposition is similarly pronounced, reaffirming the bifunctional catalytic efficacy of the Gd-doped surface. EIS was conducted to delineate the contributions of ohmic and faradaic resistances to the observed performance enhancement (Fig. 4(e)). The Nyquist plots show pristine Mn_3O_4 possesses lower charge-transfer resistance (R_{ct}), while Gd-Mn_3O_4 displays a moderately enlarged mid frequency semicircle. Though seemingly inconsistent with its superior battery performance, separates bulk electronic conductivity from intrinsic electrocatalytic activity. The slight increase in R_{ct} stems from Gd-induced lattice distortion and localized electron trap states that slightly impede bulk electron transport. Even with this minor conductive drawback, Gd-Mn_3O_4 achieves greatly boosted discharge capacity and reduced overpotential, proving its outstanding performance not rely solely on favorable bulk conductivity but originates from the Gd 4f-O 2p-Mn orbital coupling that optimizes interfacial CO_2 redox kinetics [11, 58]. Instead, the performance gains are fundamentally rooted in the altered reaction pathway, which collectively override any minor impedance penalty incurred by dopant incorporation. Finally, the long-term operational durability of the cathodes was evaluated under a constant capacity protocol of 1000 mAh·g^{-1} at 100 mA·g^{-1}, as presented in Figs. 4(f) and 4(g). The Gd-Mn_3O_4 cathode demonstrates a remarkably prolonged cycle life, sustaining stable operation for approximately 230 cycles with minimal degradation in terminal voltage before eventual fade. This endurance significantly eclipses the cycling stability of the unmodified Mn_3O_4 cathode, which succumbs to rapid capacity decay and polarization buildup due to the accumulation of recalcitrant Li_2CO_3 deposits and parasitic side reactions. Furthermore, the cycling longevity of the Gd-Mn_3O_4 nanorods surpasses that of the vast majority of most transition-metal-oxides-based catalysts reported to date, as tabulated in Table S3 in the ESM. This exceptional reversibility is directly attributable to the synergistic attributes of the Gd-O-Mn architecture, preserving the integrity of the catalytic interface and ensuring sustained mass transport throughout extended cycling.

To elucidate the mechanistic origins of the enhanced reversibility conferred by the Gd-O-Mn architecture, the phase and chemical evolution of the cathode were tracked at representative discharge and recharge states (Fig. 5(a)). X-ray diffraction (Fig. 5(b)) reveals the emergence of distinct reflections at ~22° and 32° 2θ upon discharge, diagnostic of Li_2CO_3 crystallization; these features are fully attenuated upon recharge, indicating complete product decomposition. Vibrational spectroscopy corroborates this reversibility: FTIR spectra (Fig. 5(c)) display prominent carbonate ν_2 (864 cm^{-1}) and ν_3 (1435 cm^{-1}) bands exclusively in the discharged state, while Raman spectra (Fig. 5(d)) exhibit a characteristic ν_1 symmetric stretching mode of CO_3^{2-}, which vanishes following recharge. Surface sensitive XPS further substantiates this trend. The Li 1s spectrum of the discharged cathode (Fig. 5(e)) features a component at ~55.3 eV attributable to Li_2CO_3, and the corresponding C 1s spectrum (Fig. 5(f)) shows an emergent peak at ~289.8 eV assigned to carbonate carbon; both signatures revert to near-

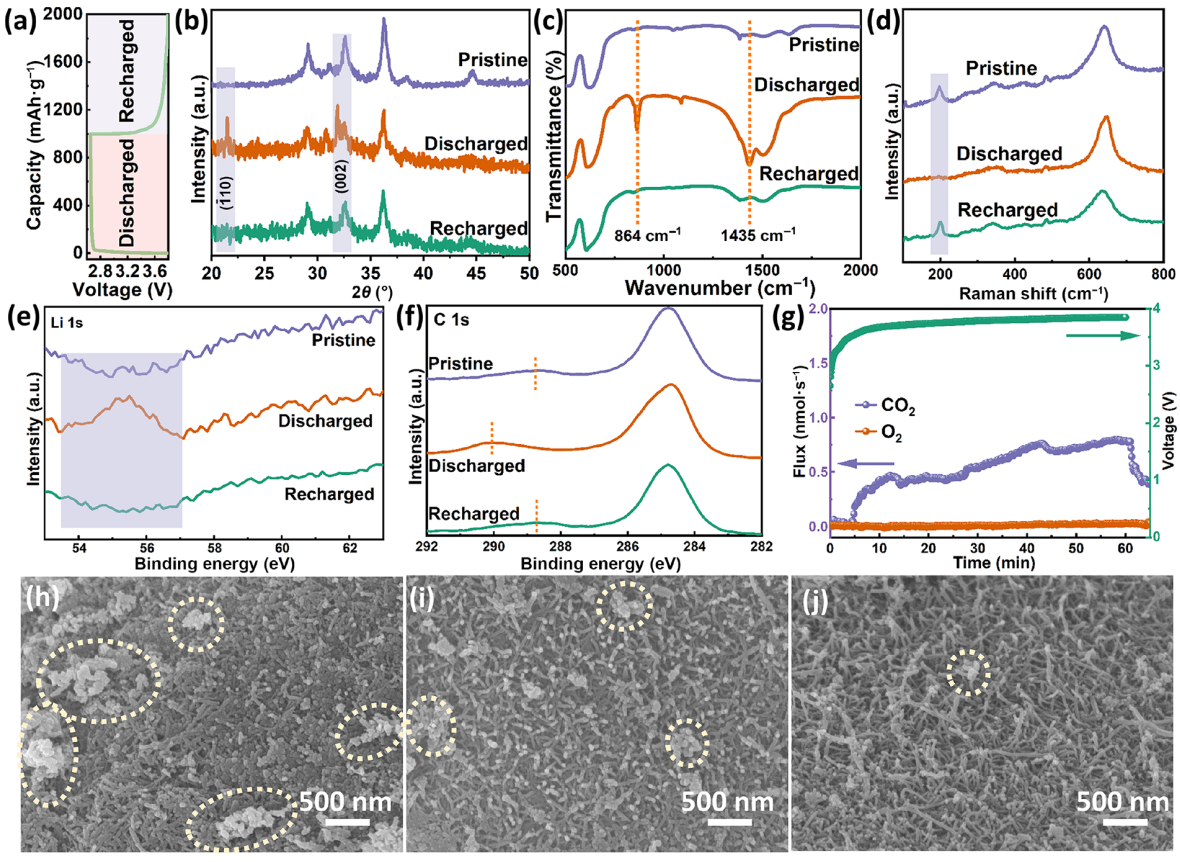

Figure 5 Characterization of Gd-Mn_3O_4 cathodes in Li-CO_2 batteries at different discharge-recharge stages. (a) Initial voltage profiles at 100 mA·g^{-1}. (b) XRD patterns. (c) FTIR spectra. (d) Raman spectra. (e, f) High-resolution Li 1s and C 1s XPS spectra. (g) *In situ* DEMS data for CO_2 evolution with recharge curves after 60 min discharge at 100 mA·g^{-1}. SEM images for (h–i) discharged and (j) recharged states, respectively.

pristine levels upon recharging. The faradaic origin of the anodic capacity was confirmed by *in situ* DEMS (Fig. 5(g)). During recharge, a pronounced CO_2 evolution transient is observed, exhibiting tight temporal correlation with the voltage plateau and yielding an electron-to-CO_2 ratio consistent with the stoichiometric decomposition of Li_2CO_3. Morphological visualization by SEM (Figs. 5(h)–5(j)) provides direct visual corroboration: the smooth nanorod surfaces of the pristine electrode become uniformly encased in a dense, particulate Li_2CO_3 film upon discharge, yet recover their original architecture upon recharge with negligible residual deposits. Collectively, these results confirm complete oxidative decomposition of Li_2CO_3 during charging, and no detectable by-products or electrolyte decomposition species are observed. The Gd-O-Mn asymmetric coordination structure thus enables rapid Li_2CO_3 nucleation and reversible breakdown, which accounts for the low overpotential and superior cycling stability of the Gd-Mn_3O_4 cathode [10, 59]. To attain a fundamental and atomistic understanding of the superior catalytic performance conferred by Gd-O-Mn architecture, DFT calculations were performed on slab models representative of the pristine Mn_3O_4 (112) and Gd-Mn_3O_4 (112) surfaces, as depicted in Figs. 6(a) and 6(b) and Figs. S6 and S7 in the ESM, respectively. Geometry optimization reveals that gadolinium incorporation induces a subtle yet significant perturbation of the local coordination environment. Specifically, the Mn-O bond distance within the immediate vicinity of the dopant undergoes a slight contraction from 1.97 to 1.96 Å, while the nascent Gd-O bond length is established at 2.31 Å, consistent with the larger ionic radius of Gd^{3+}. This asymmetric bonding configuration is anticipated to modify the local charge distribution, a hypothesis directly validated by charge density difference analysis (Fig. 6(c)). A pronounced redistribution of electron density is observed across the Gd-O-Mn bridge, manifesting as a net transfer of charge from the electropositive Gd center, traversing the intervening oxygen atom, and accumulating on the Mn site. This computational finding is in excellent agreement with the negative binding energy shift observed for Mn 2p in the XPS spectra (Fig. S3(c) in the ESM), thereby providing a robust theoretical underpinning for the experimentally deduced electron enrichment at the Mn sublattice. Such a directional electron-transfer conduit establishes an optimal electronic landscape for facilitating both the reductive activation of CO_2 and the subsequent oxidative decomposition of carbonate species. The structural robustness of the Gd-O-Mn motif was further interrogated through analysis of the electron localization function (ELF), presented in Fig. 6(d). The ELF map reveals a significant degree of electron localization within the Gd-O interatomic region, indicative of a stable, covalent-like interaction. This finding confirms that the heterometallic Gd-O-Mn linkage is not merely a metastable defect but rather constitutes a robust structural unit capable of withstanding the repeated lattice breathing and phase transformations inherent to extended electrochemical cycling. Furthermore, evaluation of the surface work function (Fig. 6(e)) demonstrates that Gd doping effectively reduces the energetic barrier for electron emission from 4.75 eV for pristine Mn_3O_4 (112) to 4.68 eV for the Gd-Mn_3O_4 (112) surface. This lowered work function implies a facilitated electron transfer capability across the cathode-electrolyte heterointerface, thereby accelerating the initial charge-transfer step of the CO_2 reduction reaction [21, 32].

To deconvolute the specific orbital contributions underpinning

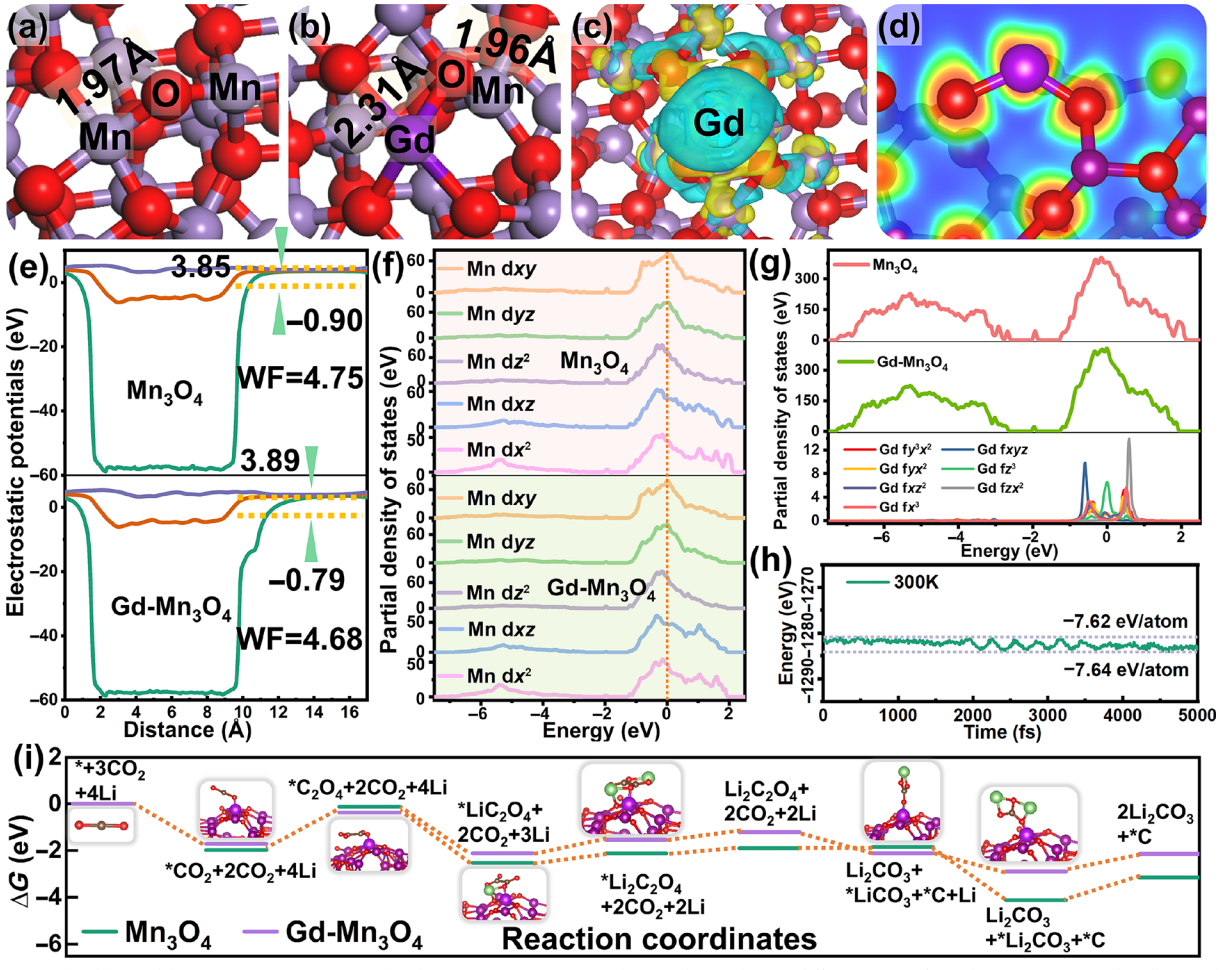

Figure 6 (a, b) Slab models pristine Mn_3O_4 (112) and Gd-Mn_3O_4 (112), respectively. (c) Charge density difference map for Gd-Mn_3O_4 (112) with yellow and green regions representing electron accumulation and depletion, respectively. (d) ELF plot of the Gd-Mn_3O_4 (112) facet. (e) Computed work functions for both Mn_3O_4 (112) and Gd-Mn_3O_4 (112) surfaces. (f, g) PDOS profiles for Mn_3O_4 (112) and Gd-Mn_3O_4 (112), respectively. (h) Free energy profile at 300 K for the Gd-Mn_3O_4 (112) surface. (i) Comparative free energy diagrams for the CO_2 to Li_2CO_3 conversion pathway on Gd-Mn_3O_4 (112).

the modified electronic structure, the projected density of states (PDOS) was computed. As illustrated in Figs. 6(f) and 6(g), the incorporation of Gd does not substantially alter the fundamental valence-band configuration or the Mn 3d orbital manifold, indicating that the intrinsic electronic character of the Mn-O framework is largely preserved. Instead, the Gd 4f states are observed to introduce localized electronic states proximal to the Fermi level, which serve to modulate the overall electronic structure and likely participate in mediating the binding interactions with CO_2 intermediates. The thermal and dynamic stability of the Gd-doped surface was further corroborated by ab initio molecular dynamics (AIMD) simulations (Fig. 6(h)), which exhibit negligible structural fluctuation or bond rupture over the simulated timescale, attesting to the thermodynamic viability of the Gd-O-Mn configuration under operational conditions. Finally, the full thermodynamic landscape covering both the discharge CO_2 reduction and reverse charging Li_2CO_3 decomposition pathways was mapped by calculating the Gibbs free energy diagrams for both pristine and doped surfaces, as shown in Fig. 6(i). For the discharge process, the free energy profile reveals that Gd-Mn_3O_4 (112) exhibits a markedly enhanced affinity for the initial adsorption of CO_2, as evidenced by a more negative adsorption free energy. Critically, the incorporation of Gd substantially lowers the kinetic barrier associated with the rate-determining step (RDS) of discharge, namely the formation of the $*C_2O_4$ intermediate, which accelerates the CO_2 reduction kinetics. For the charging CO_2 evolution process, the Gd-induced Gd-O-Mn gradient orbital coupling shifts the O 2p band center upward and accumulates extra electron density on bridging lattice oxygen. Such modulated lattice oxygen delivers stronger nucleophilic activity and significantly reduces the activation energy for breaking the C-O bonds within Li_2CO_3, enabling thorough oxidative decomposition of insulating carbonate products. This efficient reversible decomposition suppresses irreversible residue accumulation on the cathode surface and well preserves the catalytic active interface over repeated cycles, which directly explains the remarkably prolonged cycling stability observed in electrochemical tests (Fig. 4) [11, 41, 58]. Collectively, the DFT calculations provide a cohesive and multi-faceted mechanistic framework: the asymmetric Gd-O-Mn coordination induces a directional charge redistribution, strengthens the structural integrity of the catalytic interface, and optimizes the binding energetics of key reaction intermediates, thereby synergistically conferring the exceptional performance characteristics of the Gd-Mn_3O_4 cathode [4].

4 Conclusions

This work fabricates atomically asymmetric Gd-O-Mn motifs in Mn_3O_4 nanorods to build a Gd 4f-O 2p-Mn 3d gradient orbital

coupling system, resolving the kinetic drawbacks of single d-p orbital hybridization in conventional Li-CO_2 battery cathodes. Gd^{3+} doping induces local lattice distortion and directional charge transfer from Gd to Mn, elevating the O 2p band center and activating lattice oxygen redox. The cascaded electronic channel optimizes orbital matching with CO_2 and carbonate intermediates, lowering barriers for CO_2 reduction and Li_2CO_3 decomposition, and thus delivering superior capacity, low polarization and long cycling life for Gd-Mn_3O_4. More crucially, this study clarifies how rare-earth 4f electrons modulate interfacial electronic states and stabilize oxide frameworks during cycling. The proposed f-p-d gradient orbital coupling strategy provides a universal design principle for high-performance bifunctional electrocatalysts. It offers a facile orbital-regulation route via rare-earth doping, delivering clear guidance for constructing robust catalytic sites in next-generation Li-CO_2 batteries and related metal-gas energy storage devices.

Acknowledgements

This work was supported by the Anhui Provincial Education Department Youth Program (2025AHGXZK20115, 2025AHGXZK40313), the Science and Technology Program Project of Wuhu City (2024kj036), and the Talent Project of Bengbu Medical College (bsqd202555).

Declaration of conflicting interests

The authors declare no conflicting interests regarding the content of this article.

Data availability

All data needed to support the conclusions in the paper are presented in the manuscript and/or the Supplementary Materials. Additional data related to this paper may be requested from the corresponding author upon request.

Electronic Supplementary Material Supplementary material (further details of the materials, DFT computational details, TEM images, XPS spectrum) is available in the online version of this article at https://doi.org/10.26599/NRE.2026.9120264.

References

[1] Gidden, M. J.; Joshi, S.; Armitage, J. J.; Christ, A. B.; Boettcher, M.; Brutschin, E.; Köberle, A. C.; Riahi, K.; Schellnhuber, H. J.; Schleussner, C. F. et al. A prudent planetary limit for geologic carbon storage. *Nature* **2025**, *645*, 124–132.

[2] Wang, X.; Li, M.; Tang, Y. W.; Li, H.; Fu, G. T. Rare earths evoked gradient orbital coupling in electrocatalysis: Recent advances and future perspectives. *Prog. Mater. Sci.* **2026**, *155*, 101539.

[3] Zhang, S. L.; Sun, L.; Fan, Q. N.; Zhang, F. L.; Wang, Z. J.; Zou, J. S.; Zhao, S. Y.; Mao, J. F.; Guo, Z. P. Challenges and prospects of lithium-CO_2 batteries. *Nano Res. Energy* **2022**, *1*, 9120001.

[4] Pan, Q.; Ma, X. P.; Wang, H. J.; Shu, Y. M.; Liu, H. X.; Yang, L.; Li, W. Y.; Liu, J. T.; Wu, Y. C.; Mao, Y. et al. Approaching splendid catalysts for Li–CO_2 battery from the theory to practical designing: A review. *Adv. Mater.* **2024**, *36*, 2406905.

[5] Xu, Y. Y.; Xue, H. R.; Li, X. J.; Fan, X. L.; Li, P.; Zhang, T. F.; Chang, K.; Wang, T.; He, J. P. Application of metal-organic frameworks, covalent organic frameworks and their derivates for the metal-air batteries. *Nano Res. Energy* **2023**, *2*, e9120052.

[6] Sarkar, A.; Dharmaraj, V. R.; Yi, C. H.; Iputera, K.; Huang, S. Y.; Chung, R. J.; Hu, S. F.; Liu, R. S. Recent advances in rechargeable metal-CO_2 batteries with nonaqueous electrolytes. *Chem. Rev.* **2023**, *123*, 9497–9564.

[7] Xiao, X.; Zhang, Z. J.; Yan, A. J.; Hao, Y. S.; Yan, G. F.; Tan, P. Upgrading carbon utilization and green energy storage through oxygen-assisted lithium-carbon dioxide batteries. *Energy Storage Mater.* **2024**, *65*, 103129.

[8] Shen, J.; Wang, D. S. How to select heterogeneous CO_2 reduction electrocatalyst. *Nano Res. Energy* **2024**, *3*, e9120096.

[9] Mohanty, D.; Kuan, W. F. Recent advances in carbon-based electrocatalysts for rechargeable Li–CO_2 batteries: A review. *Mater. Today Energy* **2025**, *54*, 102095.

[10] Yang, Z.; Yuan, W. L.; Wang, T.; Ozoemena, K. I.; Eliseeva, S.; Wu, Y. P. Heterostructures for advanced rechargeable batteries. *Energy Z* **2026**, *2*, 200010.

[11] Li, S.; Li, S. Y.; Wang, J.; Wu, Y. J.; Yan, J.; Liu, K.; Yang, Y. H.; Su, H. Axial electron-conduction engineering of single-atom copper catalyst for kinetic-fast oxygen reduction. *Energy Mater.* **2026**, *6*, 600058.

[12] Lu, B. Y.; Wu, X. R.; Xiao, X.; Chen, B.; Zeng, W. H.; Liu, Y. Q.; Lao, Z. J.; Zeng, X. X.; Zhou, G. M.; Yang, J. L. Energy band engineering guided design of bidirectional catalyst for reversible Li–CO_2 batteries. *Adv. Mater.* **2023**, *36*, 2308889.

[13] Qi, R. Y.; Shi, Y. L.; Tang, W. H.; Liu, T. L.; Gao, L.; Teng, K. W.; Liu, R. P. Bimetallic phosphides-oxides heterostructures coupled heteroatom-doped carbon as bifunctional electrocatalysts for Zn-air batteries. *Nano Res. Energy* **2025**, *4*, e9120151.

[14] Qiu, J. H.; Wang, M.; Liu, Y. Q.; Song, Y. Z.; Yang, Z. L.; Chen, Y. L.; Lu, B. Y.; Tao, X.; Yang, J. L.; Zhou, G. M. Asymmetric structure-induced d-orbital splitting boosts highly active and stable Li–CO_2 batteries. *Angew. Chem., Int. Ed.* **2025**, *64*, e202516978.

[15] Chen, X. Y.; Chen, J.; Qiao, Y.; Gao, Y.; Fan, S. W.; Liu, Y. J.; Li, L.; Liu, Y.; Chou, S. L. Facile fabrication of Ni, Fe-doped δ–MnO_2 derived from Prussian blue analogues as an efficient catalyst for stable Li–CO_2 batteries. *Chem. Sci.* **2024**, *15*, 2473–2479.

[16] Li, J. T.; Liu, L. M.; Guan, D. H.; Liang, H.; Lu, Z. C.; Wang, H.; Zhang, Y. W.; Tang, J. M.; Chen, S. H.; Feng, G. D. et al. *d-p* orbital hybridization tailoring for boosted redox kinetics in Li–CO_2 batteries. *Adv. Funct. Mater.* **2026**, *36*, e14223.

[17] Li, X.; Zhang, G. L.; Zhang, D. M.; Yang, R. N.; Yu, H.; Zhang, X. Q.; Lian, G.; Hou, H.; Guo, Z. H.; Hou, C. X. et al. A high-entropy cathode catalyst with multiphase catalytic capability of Li_2O_2 and Li_2CO_3 enabling ultralong cycle life in Li-air batteries. *Energy Environ. Sci.* **2024**, *17*, 8198–8208.

[18] Deng, Q. H.; Yang, Y.; Mao, C. F.; Wang, T. Y.; Fang, Z.; Yan, W. W.; Yin, K.; Zhang, Y. W. Electronic state modulation and reaction pathway regulation on necklace-like MnO_x–CeO_2@polypyrrole hierarchical cathode for advanced and flexible Li–CO_2 batteries. *Adv. Energy Mater.* **2022**, *12*, 2103667.

[19] Wang, X.; Wang, J. W.; Wang, P.; Li, L. C.; Zhang, X. Y.; Sun, D. M.; Li, Y. F.; Tang, Y. W.; Wang, Y.; Fu, G. T. Engineering 3d-2p-4f gradient orbital coupling to enhance electrocatalytic oxygen reduction. *Adv. Mater.* **2022**, *34*, 2206540.

[20] Liu, W.; Liang, Y.; Huo, M. T.; Xi, J.; Gu, X. W.; Ma, N.; Wang, M. Y.; Xing, Z. H.; Chang, J. F. Asymmetric Fe–N_4–O sites enabled by axial oxygen coordination for high-efficiency Zn-air batteries. *Nano Res. Energy* **2026**, *5*, e9120232.

[21] Ran, Y.; Xu, C. F.; Ji, D. Y.; Zhao, H. P.; Li, L. Q.; Lei, Y. Research progress of transition metal compounds as bifunctional catalysts for zinc-air batteries. *Nano Res. Energy* **2024**, *3*, e9120092.

[22] Yang, B. Y.; Li, K.; Yang, C. Y.; Zhang, Y. H.; Gong, Y. Orbital hybridization and electron transfer triggered by V-dopant and symmetry breakage to stabilize low-valent Mn for zinc-ion batteries. *Chem. Eng. J.* **2025**, *513*, 163032.

[23] Liang, N.; Zhu, Q.; Jiang, M. P.; Hou, X. Y.; Shao, Z. Y.; Wang, S. H.; He, Y. Z.; Zhang, W. Y.; Huang, R. L.; Zhang, Y. W. et al. Self-aligned $BiFeO_3$ polarization vector induced by MnO_6 octahedral Jahn-Teller distortion for enhanced photocatalytic CO_2 reduction. *J. Am. Chem. Soc.* **2025**, *147*, 43380–43390.

[24] Wang, Y. X.; Zhou, H.; Wei, S. Q.; Chen, S. M.; Cao, D. F.; Zhou, Q.; Wu, X. J.; Song, L. Boosting ion transport in manganese dioxide cathodes through electronically tuned molecular intercalants. *J. Am. Chem. Soc.* **2025**, *147*, 41297–41307.

[25] Wang, Y.; Fang, W. S.; Zhu, D. Y.; Chen, J. W.; Wang, X.; Park, H. S.; Liu, J. H.; Xia, B. Y. Recent progress in rare earth element modulated electrocatalysts for CO_2 electroreduction. *Prog. Mater. Sci.* **2026**, *157*, 101594.

[26] Zhuang, Y.; Hu, F.; He, D.; Yu, J.; Chen, Q.; Peng, L. Weakening the oxophilicity of PtGd alloy via nitrogen-induced 5d/4f-2p orbital interaction for efficient fuel cell cathode performance. *Adv. Funct. Mater.* **2026**, *36*, e24485.

[27] Lin, B. X.; Zhang, Y. Y.; Li, W. F.; Huang, J. K.; Yang, Y.; Or, S. W.; Xing, Z. Y.; Guo, S. J. Recent advances in rare earth compounds for lithium-sulfur batteries. *eScience* **2024**, *4*, 100180.

[28] Li, C. Y.; Wang, P.; He, M.; Yuan, X. L.; Fang, Z.; Li, Z. X. Rare earth-based nanomaterials in electrocatalysis. *Coord. Chem. Rev.* **2023**, *489*, 215204.

[29] Li, M.; Wang, X.; Liu, K.; Sun, H. M.; Sun, D. M.; Huang, K.; Tang, Y. W.; Xing, W.; Li, H.; Fu, G. T. Reinforcing Co–O covalency via Ce(4f)–O(2p)–Co(3d) gradient orbital coupling for high-efficiency oxygen evolution. *Adv. Mater.* **2023**, *35*, 2302462.

[30] Zhu, Y.; Wang, Y. J.; Zhou, Y.; Chen, M. H.; Wang, X.; Li, M.; Wang, Y.; Tang, Y. W.; Li, H.; Wei, L. et al. Ordered Ba_2EuIrO_6 double perovskite with active Ir–O_{bri}–Eu unit for enhanced electrocatalytic oxygen evolution in PEMWE. *Angew. Chem., Int. Ed.* **2026**, *65*, e8724105.

[31] Deng, Q. H.; Wang, T. Y.; Yang, Y. Gradient 4f-2p-3d orbital coupling activates interfacial asymmetric Co–O–Ce sites towards enhanced bidirectional catalysis in Li–CO_2 batteries. *Energy Storage Mater.* **2026**, *86*, 104992.

[32] Zhang, H. Y.; Wang, X. J.; Sun, Y. F.; Wang, X. X.; Tang, Z.; Li, S. Y.; Gao, X. Y.; Wang, J. R.; Hou, Z. S.; Nie, K. Q. et al. Targeted C–O bond cleavage of *CH_2CHO at copper active sites for efficient electrosynthesis of ethylene from CO_2 reduction. *Appl. Catal. B: Environ. Energy* **2024**, *351*, 123992.

[33] Yang, L. T.; Bai, J. S.; Zhang, N. S.; Jiang, Z.; Wang, Y.; Xiao, M. L.; Liu, C. P.; Zhu, S. Y.; Xu, Z. J.; Ge, J. J. et al. Rare earth evoked subsurface oxygen species in platinum alloy catalysts enable durable fuel cells. *Angew. Chem., Int. Ed.* **2024**, *63*, e202315119.

[34] Wang, X. M.; Li, N.; Wang, G. C.; Liu, M.; Zhang, C.; Liu, S. X. Ultrafine nanoclusters unlocked 3d-4f electronic ladders for efficient electrocatalytic water oxidation. *ACS Nano* **2024**, *18*, 20518–20529.

[35] Tang, Y. W.; Liu, H. L.; Zhu, X.; Liu, M. T.; Tang, W. J.; Wei, G. X.; Feng, Y. H.; Xiao, B.; Wang, P. F. Restraining the Jahn-Teller distortion in Mn-based layered cathodes toward high-performance potassium-ion batteries. *ACS Nano* **2025**, *19*, 21118–21129.

[36] Wang, H. L.; An, J. J.; Zhao, W. X.; Yu, B. K.; Li, Y.; Hu, J. Q.; Jiang, S. K.; Gu, Q. F.; Zhu, J. W.; Zhu, H. et al. Constructing heterotransition metal ligand field clusters with a compact spatial structure for maintaining unimpeded sodium-ion migration. *ACS Nano* **2025**, *19*, 34966–34980.

[37] Xiao, W.; Yoo, K.; Kim, J. H.; Xu, H. Y. Decoupling redox kinetics with complementary d-band catalysis for high-performance lithium-sulfur batteries. *ACS Nano* **2025**, *19*, 23223–23234.

[38] Li, M.; Wang, Y.; Zheng, Y.; Fu, G. T.; Sun, D. M.; Li, Y. F.; Tang, Y. W.; Ma, T. Y. Gadolinium-induced valence structure engineering for enhanced oxygen electrocatalysis. *Adv. Energy Mater.* **2020**, *10*, 1903833.

[39] Li, Y. P.; Liu, X. R.; Wang, H. H.; Liu, S.; Chen, D. R.; Jiao, X. L.; Xia, Y. G. Dual-orbital synergy and alkali metal modulation: Harnessing Cu–Gd *d-f* coupling for enhanced CO_2 reduction with regulated hydrogenation selectivity. *Adv. Funct. Mater.* **2026**, *36*, e10561.

[40] Wang, Y.; Liu, Y. D.; Liu, S. J.; Qin, Y. P.; Liu, J. F.; Jia, X.; Jiang, Q. L.; Wang, X.; Zhao, Y. Z.; Liu, L. et al. Gd-induced oxygen vacancy creation activates lattice oxygen oxidation for water electrolysis. *Adv. Funct. Mater.* **2025**, *35*, 2500118.

[41] Zhu, X. Q.; Zheng, R. X.; Yang, M. M.; Xu, J.; Niu, X. B.; Cheng, J. L.; Ding, D.; Wang, B. High-entropy Prussian blue analogues enable synergistic electronic coupling and charge compensation for efficient Li–CO_2 batteries. *Adv. Funct. Mater.* **2026**, *36*, e10533.

[42] He, C.; Lee, C. H.; Meng, L.; Chen, H. Y. T.; Li, Z. Selective orbital coupling: An adsorption mechanism in single-atom catalysis. *J. Am. Chem. Soc.* **2024**, *146*, 12395–12400.

[43] Hu, D. X.; Wang, Y. J.; Chen, W. H.; Jiang, Z. Q.; Deng, B. L.; Jiang, Z. J. Strong metal-support interaction modulation between Pt nanoclusters and Mn_3O_4 nanosheets through oxygen vacancy control to achieve high activities for acidic hydrogen evolution. *Small* **2024**, *20*, 2402652.

[44] Chen, J.; Li, J. S.; Kondratenko, V. A.; Wu, K.; Zanina, A.; Jiang, W.; Li, Y. M.; Jiang, G. Y.; Kondratenko, E. V. Steady-state and transient kinetic studies of origins affecting the efficiency of oxidative coupling of methane over Ba/Gd_2O_3 catalysts. *ACS Catal.* **2025**, *15*, 2760–2771.

[45] Deng, S. Z.; Xu, B. G.; Liu, X. L.; Yang, Y. J.; Xiao, Y. N.; Wang, S.; Zhao, J. X.; Chen, T. D. Cationic vacancy modulation of Mn_3O_4 as a superior cathode for durable aqueous Zinc-ion batteries. *Adv. Funct. Mater.* **2025**, *35*, 2413711.

[46] Xu, C. Y.; Yu, H. Z.; Huang, H. M.; Li, S.; Cao, Y. H.; Peng, W. W.; Li, Y. T.; Ke, H. J.; Xu, S. Y.; Mo, H. X. et al. Hydroxyl spillover activated from the strongly coupled Ru@Mn_3O_4 heterostructure to promote alkaline hydrogen evolution. *Angew. Chem., Int. Ed.* **2025**, *64*, e202504667.

[47] Ning, S. W.; Li, M.; Wang, X.; Zhang, D.; Zhang, B. Y.; Wang, C. K.; Sun, D. M.; Tang, Y. W.; Li, H.; Sun, K. et al. Importing antibonding-orbital occupancy through Pd–O–Gd bridge promotes electrocatalytic oxygen reduction. *Angew. Chem., Int. Ed.* **2023**, *62*, e202314565.

[48] Patel, S. K. S.; Dhak, P.; Kim, M. K.; Lee, J. H.; Kim, M.; Kim, S. K. Structural and magnetic properties of Co-doped Gd_2O_3 nanorods. *J. Magn. Magn. Mater.* **2016**, *403*, 155–160.

[49] Li, Z. Q.; Chen, X.; Yao, G.; Wei, L. Z.; Chen, Q. W.; Luo, Q. Q.; Zheng, F. C.; Wang, H. Strengthening d-p orbital-hybridization via coordination number regulation of manganese single-atom catalysts toward fast kinetic and long-life sodium-sulfur batteries. *Adv. Funct. Mater.* **2024**, *34*, 2400859.

[50] Kumar, A.; Lee, J.; Kim, M. G.; Debnath, B.; Liu, X. H.; Hwang, Y.; Wang, Y.; Shao, X. D.; Jadhav, A. R.; Liu, Y. et al. Efficient nitrate conversion to ammonia on f-block single-atom/metal oxide heterostructure via local electron-deficiency modulation. *ACS Nano* **2022**, *16*, 15297–15309.

[51] Wang, B.; Xing, Z. Q.; Jia, S. Y.; He, Q.; Zhao, Y.; Meng, X. K.; Tang, S. C. Coupling ultrafine transition metal and rare earth oxide nanocrystals toward highly active and stable catalysts for lithium-sulfur batteries. *ACS Nano* **2025**, *19*, 15120–15129.

[52] Liu, H. J.; Jiang, Y.; Jiang, K. H.; He, K.; Zhong, Z. Y.; Gu, C.; Du, Y. P. In-plane creation of rare earth-induced spin filtering effect in ultrathin nanosheets for enhanced water oxidation. *Adv. Funct. Mater.* **2026**, *36*, e25512.

[53] Liu, Y.; Zhang, L.; Xu, Q. L.; Zhang, S. J.; Zhou, Y. T.; Hu, G. Z. Oxophilic low-coordination Gd–N_3 single atom sites with P-enhanced second coordination for high-performance Al-air batteries. *Adv. Funct. Mater.* **2025**, *35*, 2413134.

[54] Liu, Z. W.; Wang, Z. W.; Lv, D. D.; Yang, H. Y.; Kang, Z. H.; Ghosh, S.; Menezes, P. W.; Chen, Z. L. Efficient electrosynthesis of hydrogen peroxide enabled by a hierarchical hollow RE–P–O (RE = Sm, La, Gd) architecture with open channels. *Adv. Mater.* **2025**, *37*, 2311997.

[55] Chen, W. P.; Bai, K. P.; Lv, M. T.; Ni, S.; Huang, C.; Yang, Q. Y.; Zheng, Y. Z. Porous 3d-4f coordination clusters for selective visible-light photocatalytic CO_2 reduction to CO. *Angew. Chem., Int. Ed.* **2025**, *64*, e202424805.

[56] Liu, W. Q.; Bai, P. Y.; Wei, S. L.; Yang, C. C.; Xu, L. Gadolinium changes the local electron densities of nickel 3d orbitals for efficient electrocatalytic CO_2 reduction. *Angew. Chem., Int. Ed.* **2022**, *61*,

e202201166.
[57] Sun, L.; Gu, Q. F.; Yuwono, J. A.; Zhou, J. W.; Johannessen, B.; Zhao, L. F.; Zhang, C. F.; Li, G. J.; Guo, Z. P.; Zhang, S. L. High-performance aprotic Li–CO_2 battery enabled by the Ru heterophase catalyst. *ACS Nano* **2025**, *19*, 20051–20062.
[58] Li, X. L.; Wang, X.; Yang, M. M.; Meng, H. B.; Yuan, J.; Yi, Q.; Cao, Z. H.; Hou, K.; Qi, K.; Gao, L. L. et al. Interlayer expanded MXene film cathodes with rich defects for flexible 2-electron oxalate-based Li–CO_2 batteries: A new path to enhanced energy efficiency and durability. *Adv. Mater.* **2025**, *37*, 2500064.
[59] Zhao, Z. W.; Wu, Y. Y.; Yao, T. F.; Pang, L.; Liu, J. L.; Feng, X.; Peng, Z. Q. Revealing redox-mediated CO_2 reduction reaction mechanisms in aprotic Li–CO_2 batteries. *Adv. Mater.* **2025**, *37*, 2506880.

Qinghua Deng serves as Director of the Wuhu R&D Center for Energy Conversion and Storage Materials at Wuhu Vocational Technical University. He was awarded his Ph.D. degree in Materials Physics and Chemistry from Southeast University in 2024 and was recognized as a High-Level Talent of Wuhu City. His research focuses on energy conversion and storage materials as well as their device engineering, with particular emphasis on the development of advanced metal-gas batteries. As the first author, he has published >10 SCI papers in leading journals including *Advanced Energy Materials*, *Energy Storage Materials*, *Chemical Engineering Journal*, and *Small*.

Yahui Wu a Youth Editorial Board Member of *Nano Research Energy*, is currently a Lecturer at Bengbu Medical University. From 2019 to 2025, he conducted his doctoral and postdoctoral research at the Chinese Academy of Sciences under the supervision of Academician Buxing Han. His research focuses on the rational design of functional catalysts for electrocatalytic CO_2 reduction. He has been awarded the BMS Junior Fellow and grants from the China Postdoctoral Science Foundation, and has published several first-author SCI papers in prestigious journals, including *Angewandte Chemie International Edition*, *Chemical Science*, *Nano Research*, *Green chemistry* and *Carbon Energy*.